J. Fluid Mech. (1986), *vol.* 172, *pp.* 373–399
Printed in Great Britain

Laboratory observations of a gravity current on a sloping bottom: the generation of shelf waves

By JOHN A. WHITEHEAD AND DAVID C. CHAPMAN
Woods Hole Oceanographic Institution, Woods Hole, MA 02543, USA

(Received 21 October 1985 and in revised form 12 May 1986)

A source of light water was started along the outside vertical wall of a cylindrical tank in uniform rotation. Like wall gravity currents studied previously, it had a nose which detrained eddies as it propagated. The gravity current then impinged upon a sloping bottom with the following effects: (i) the gravity current became more laminar; the detrainment of eddies at the nose and off the side of the current ceased; (ii) the gravity current became wider; (iii) the gravity current suddenly slowed and then continued to decelerate; (iv) when the gravity current was slower than the first-mode barotropic shelf wave, a shelf wave was radiated ahead of the gravity current; and (v) the deceleration was significantly greater than the deceleration of a gravity current next to a vertical wall. This is probably attributable to shelf-wave radiation drag, viscous effects and a finite energy source, although the relative importance of each remains an open question.

1. Introduction

Flows of low-salinity water are often emitted into the ocean in an unsteady way from bays, straits or rivers, due to winds, tides, sea-level changes and unsteady river runoff. A clear example is the flow of fresh water of Baltic origin from the Skagerrak, which is occasionally completely stopped by winds, principally when they are from the west. As the winds abate, the fresh water pours out of the Skagerrak and a gravity current of low-salinity water flows first along the southern and later along the western coast of Norway (Mork 1981). The leading edge or nose of the gravity current is a distinct low-salinity wedge of water which is found above the denser surrounding water. More importantly, in the Northern Hemisphere it is held to the right-hand coast (looking downstream) by the Earth's rotation.

A considerable amount is known about gravity currents (also called density currents) in non-rotating fluids (e.g. Simpson 1982). However, until recently, virtually nothing was known about such currents in rotating fluids. Stern (1980) analysed the characteristics of long disturbances on a density current with its nose next to a vertical wall. This led to some laboratory observations of such a gravity current and to the subsequent theoretical prediction of nose properties in which a modification of Benjamin's theory of non-rotating density currents was reconciled with rotational constraints and the behaviour of certain characteristics to predict an upstream current width and nose speed (Stern, Whitehead & Hua 1982). The current was also found to be characterized by the lateral detrainment† of eddies. The laboratory experiment exhibited reasonable agreement with the theory.

† The word detrainment has been adopted because the eddies detach from the current and stop compared to the current, in contrast to eddies in non-rotating jets and plumes which entrap surrounding fluid and continue to travel with the current.

Griffiths & Hopfinger (1983) have more recently conducted a second series of studies of a gravity current next to a vertical wall. They observed the structure of the nose to be more three-dimensional and intermittent, with the frequency of eddy-shedding at the nose often being greater than the Coriolis frequency. They present evidence that this produces vortex and wavelike motions which radiate deep into the lower fluid, and that the nose velocity has an exponential decay which was attributed to radiation of momentum by inertial waves.

Gravity currents in the ocean typically flow along a coast with variable topography rather than a vertical wall. However, no previous studies have considered gravity currents moving along a shelf with a sloping bottom. Here, results of laboratory experiments are reported which reveal some new features of such currents. First, the general character of a gravity current flowing next to a vertical wall is reviewed in §2. Then the present experiments are described in §3 followed by the results in §4. The experiments show that a gravity current over a shelf with a sloping bottom is wider, more laminar, slower and more rapidly decelerating than a gravity current next to a vertical wall. In addition, under suitable conditions barotropic shelf waves will be radiated over the shelf ahead of the gravity current and may contribute to its deceleration. Calculations of such waves are made and compared with observations.

2. Previous experiments

The two recent experimental studies (Stern *et al.* 1982; Griffiths & Hopfinger 1983), plus associated theoretical considerations have illuminated the size and speed of gravity currents next to a vertical wall. In both experiments, gravity currents were made by a 'dam-break' procedure, in which fluid of a given density was slowly added to the top of fluid of greater density in a reservoir behind a removable sliding gate. The bottom of the gate was left open, so the lower water could migrate out to the test area as the filling procedure was underway. Thus, the lower fluid remained almost motionless and in hydrostatic equilibrium. As the test run began, the gate was removed and cine film or photographs were taken of the top and side views of the resulting flow. The front that initially occupied the space vacated by the dam gate exhibited a gravitational slump accompanied by a Coriolis force-induced curve to the right. The rightward curving current of lighter fluid encountered the right-hand wall where it was deflected to the left. This process produced a gravity current which started with speed

$$U_{\mathrm{N}} \approx U_0(g^*H)^{\frac{1}{2}}, \tag{2.1}$$

where $g^* = g\Delta\rho/\rho$ is gravitational acceleration reduced by the normalized density difference, and H is the depth of the top fluid in the reservoir. U_0 was reported to be 1.0 ± 0.1 by Stern *et al.* (using their table 1 and the three largest Reynolds numbers) and 0.93 ± 0.14 by Griffiths & Hopfinger. The current had width l given by

$$l \approx L_0(g^*h_{\mathrm{u}}/f^2)^{\frac{1}{2}}, \tag{2.2}$$

where f is the Coriolis parameter, h_{u} the depth of the gravity current upstream of the nose, and L_0 was measured to be 0.5 ± 0.1 by Stern *et al.* and 0.6 ± 0.1 by Griffiths & Hopfinger. Both U_0 and L_0 were constants only for large Reynolds number and large hydrostatic number (see §4).

The gravity current also possessed a characteristic shape with a nose which shed eddies sideways and downward, a neck behind the nose which was typically thinner

and shallower than the maximum width and depth of the nose, and a current upstream which was laminar next to the wall with slower 'detached' eddies offshore. As the current flowed along the wall, it retained the above features, except that viscosity made the current more laminar far from the nose. Moreover, Griffiths & Hopfinger reported an exponential attenuation of speed with the time constant

$$t = (25 \pm 5)\left(\frac{A_0}{g^* H f}\right)^{\frac{1}{3}}, \tag{2.3}$$

where A_0 is the surface area of the upstream reservoir and a penetration length of

$$L_p = (22 \pm 4)\left[(g^* H)^{\frac{1}{2}} \frac{A_0}{f}\right]^{\frac{1}{3}}. \tag{2.4}$$

They attributed this decay to inertial wave radiation. The features of the above currents (speed, width and attenuation) will be compared with the currents in the present study.

3. Present experiments

Three sets of experiments have been performed, each with a different apparatus. The first was meant to be a preliminary experiment for the purpose of planning the final experiments, but it nonetheless yielded useful information concerning the speed of the gravity currents. Using a slightly different procedure, the second experiment was a more systematic parameter study which yielded quantitative data of nose speed and attenuation rate, as well as clear indications of shelf-wave generation. The third experiment was designed for improved visualization of shelf-wave structures and propagation speeds.

3.1. *Experiment I*

The first apparatus (figure 1*a*) consisted of a sloping false bottom with the right end (looking onshore) suitably curved so that it would butt the sidewall of an 89.8 cm diameter cylindrical tank to which it was smoothly taped. The opposite end was square and had a vertical Plexiglas wall clamped to it. The false bottom had a slope of 1:5 and intersected the free surface when the tank was filled with 10 cm of salt water. Lines drawn every 30 cm and ticks every 10 cm on the false bottom served as lengthscales. The entire apparatus was mounted on a 1 m diameter rotating turntable. The gravity current was produced by introducing a fluid at a constant rate at the side of the cylindrical wall opposite from the chord of intersection of the false bottom and the free surface (figure 1*a*). The fluid was introduced through a 9.0 cm diameter inverted funnel which had a thin sheet of foam rubber taped to it such that there was no leakage between the rim of the funnel and the foam. Dyed water was fed into the funnel from an overhead tank at a rate controlled by an adjustable valve. Runs were conducted by spinning up the water in the tank for at least 20 min, and then opening a valve in the dyed water system. A gravity current would form on the outer wall, move counterclockwise as it leaned against the outer wall, and ultimately encounter the sloping bottom where the shelf gravity current of interest would form.

The speed of the current nose was measured by noting the time that the gravity current passed markers spaced 10 cm apart on the vertical wall and on the sloping bottom. The other dimensions and the qualitative structure of the gravity current over the sloping bottom were recorded with photographs taken from above.

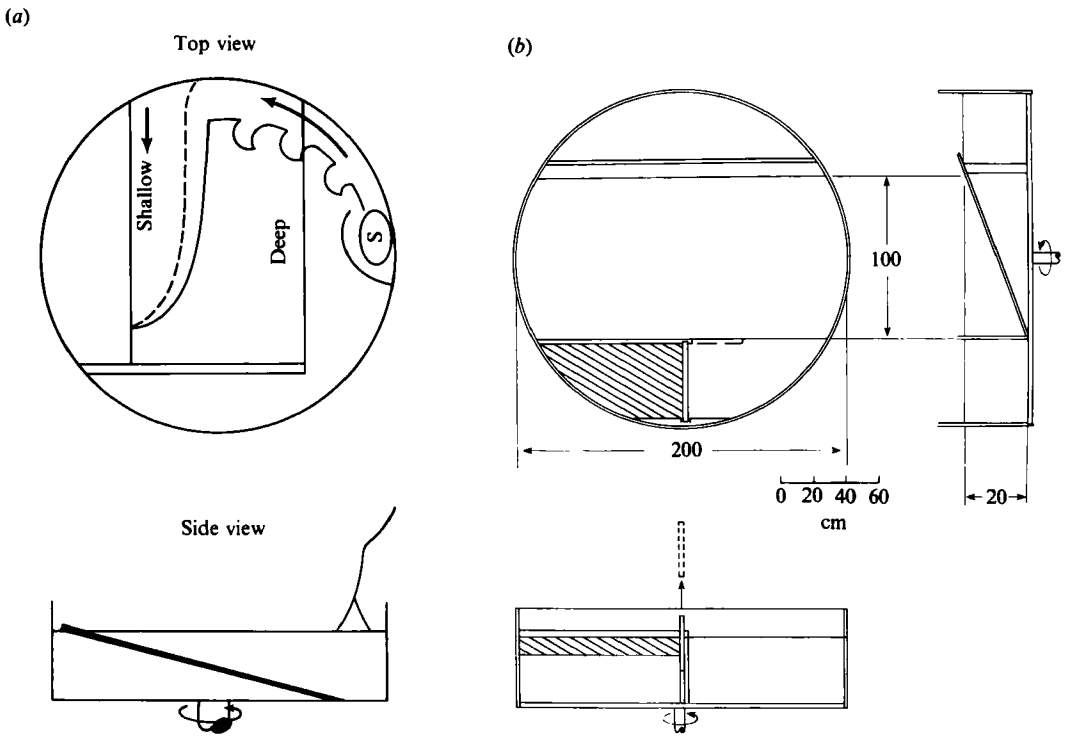

FIGURE 1. The apparatus used to observe the density current over a sloping bottom. (*a*) Experiment I. The side view shows the false bottom emplaced in the salty water on the turntable. The inverted funnel in contact with the water surface on the right serves as a source of fresh water. The top view shows schematically the shelf, the source (labelled S), and the turbulent gravity current over the shelf. The dashed line is the intersection of the edge of the current with the bottom and the solid line is the intersection with the surface. (*b*) Experiments II, III. The cross-hatch denotes dyed fresh water of depth H floating above clear salty water. The short dashed line represents the removed sliding gate. The long dashed line is the extra offshore wall in experiment III. The vertical scale has been exaggerated by a factor of two.

3.2 *Experiment II*

The second apparatus (figure 1*b*) was constructed on the 2 m diameter rotating turntable at the Coastal Research Center of the Woods Hole Oceanographic Institution. At the centre of the tank was a sloping false bottom constructed of plywood whose right-hand edge (looking onshore) was fitted to the wall of the tank and sealed with tape. An upstream reservoir was constructed with a vertical false wall and a sliding gate that extended between the false wall and the outer cylindrical wall of the turntable. The surface area of the reservoir was $A_0 = 2740$ cm^2. The bottom of the gate was open to a height of 10 cm above the bottom to allow adjustment of the fluid during the filling of the tank.

The experimental procedure was to fill the tank with water of a desired salinity to 20 cm depth and to spin it up. Fresh water was then floated above the salty water in the reservoir section by slowly introducing it onto a floating piece of wood (a standard filling procedure). The fresh water was dyed so that it could be seen after leaving the reservoir. After a time interval long enough to assure spin-up of all fluids, the sliding gate was removed and a gravity current was observed to flow along the outer wall of the tank, leaning to the right. It appeared qualitatively similar to the

gravity currents next to a vertical wall studied by Stern *et al.*, by Griffiths & Hopfinger, and in experiment I. After the gravity current reached the shelf with the sloping bottom, the fluid would pile up (as in experiment I) and spread along the coast. The experiment continued until the gravity current moving along the coast either stopped or reached the far (downstream) wall.

Data were recorded by taking 35 mm colour slides at equally spaced intervals with a camera which was synchronously rotating above the tank. A towed injector manifold was used to emplace dye lines before the run. Five different colours were injected in lines normal to the coast at 10, 50, 100, 150, and 200 cm from the upstream end of the coast in order to observe the flows of the water ahead of and beside the density current.

3.3 *Experiment III*

The third apparatus and procedure were nearly identical to the second (§3.2) except for three features. First, visualization was improved by using a thymol blue water solution with electrode wires mounted above the bottom. The wires were spaced parallel to the right-hand sidewall at distances of 10, 50, 90, 120 and 160 cm from it, and parallel to the coast at distances of 10, 30, 50, 72 and 83 cm from it. Second, the offshore false wall was extended 30 cm beyond the removable gate so that the deep edge of the false bottom was next to a vertical wall. Third, the tank was covered with transparent plastic during each run to reduce any undesirable 'wind' effects due to the rotation of the tank. The remaining procedure was identical to that of experiment II.

4. Results

In each of the experiments there were five independent variables; g^* the reduced gravity, H the depth of the top fluid in the reservoir (or in experiment I the inflow rate Q), T the rotation period, L the shelf width and ν the kinematic viscosity. (Note that in experiment I, H is the depth of the gravity current moving along the vertical wall.) To simplify the discussion, these variables may be combined to form three independent dimensionless numbers which are expected to be important in the present experiments.

The previous experiments of gravity currents next to a vertical wall showed that U_0 and L_0 in (2.1) and (2.2), respectively, were sensitive to two dimensionless numbers. The first is the hydrostatic number (Stern *et al.* 1982) which is the ratio of the Rossby radius of deformation, R (based on depth of the top fluid in the reservoir H) to H; $R/H = (g^*H/f^2)^{\frac{1}{2}}/H = (g^*/f^2H)^{\frac{1}{2}}$. It represents the expected ratio of horizontal to vertical lengthscales and is large in most oceanic and atmospheric situations. Both Stern *et al.* and Griffiths & Hopfinger reported a strong dependence of current width on R/H for $R/H \lesssim 1$, but the data support an asymptotic limit for $R/H \gg 1$. Thus, it is desirable to make R/H as large as possible. The nose velocity dependence also exhibited scatter as the hydrostatic number was varied, but the behaviour was not systematic. The second dimensionless number is the Reynolds number; $Re = (g^*H^3/\nu)^{\frac{1}{2}}$. Stern *et al.* found a slight sensitivity of nose speed to Re in the range 2000 to 6000, although this dependence was not revealed in the observations of initial velocity made by Griffiths & Hopfinger. Nevertheless, viscosity will certainly become important for small Re. Griffiths & Hopfinger clearly saw more attenuation when their Ekman number ($Re \cdot R/H$) was less than 10^{-3}. Thus, it is apparently important that $Re > 10^3\, R/H$ to eliminate the dependence on viscosity.

Run	Period (s)	g^*	Length (cm) 10	20	30 Time (s)	40	50
1	26.0	7.8	3	8	13	19	25
2	11.0	7.3	4	9	14.5	20	28
3	5.4	6.9	8	24	44	74	—
4	7.5	6.4	5	12	21	32	46
5	9.5	5.9	6	12	19	26	36
6	14.5	5.4	5	10	16	23	32
7	11.0	4.9	4	8	12	16	20
8	5.95	7.8	8	20	32	48	—
9	6.5	7.5	5	12	19	32	45
10	7.2	7.2	5	10	17	26	36
11	5.0	6.9	10	24	38	52	92
12	5.2	6.7	9	27	40	92	—

TABLE 1. Data from experiment I. Listed for each run are the rotation period, reduced gravity g^* and the time (after impinging on the sloping bottom) at which the nose of the gravity current had attained various lengths.

The third dimensionless number is the ratio of the Rossby radius of deformation to the shelf width, R/L, which represents the horizontal scale of the motion relative to the shelf width.

In general, it is desirable to make H large so that Re is large. But large H implies a small hydrostatic number which is undesirable. Furthermore, the parameter choices must also represent a compromise between the desirable values and the physical limitations of the laboratory apparatus. For example, certain experimental inconveniences should be avoided such as mixing of waters during set-up and a sizeable parabolic free surface at rapid rotation rates. Ultimately, the values of g^* varied from 4 to 16 cm/s^2, T from 5 to 26 s and H from 4 to 16 cm. The shelf width was held fixed and the kinematic viscosity was that of water at room temperature or 0.01 cm^2/s. Thus, the final experiments were possible for $Re > 10^3$ but for hydrostatic numbers of only about one.

The results of the three experiments are separated into two categories. First, results pertaining to the observed properties of the gravity current itself are described in §4.1. Then, the results showing the generation of barotropic shelf waves ahead of the gravity current are presented in light of some theoretical considerations in §4.2. The reader should keep in mind, however, that the two categories are not independent, i.e. the gravity current itself is intimately related to the radiation of barotropic shelf waves.

4.1. *Gravity-current properties*

In experiment I, twelve runs were conducted with all parameters the same for each run except (i) the rate of rotation which varied by a factor of three and (ii) the density difference which varied by approximately 50 % (table 1). For all runs the source volume flux and water depth were held fixed at $Q = 38$ cm^3 s^{-1} and $H_0 = 10$ cm, respectively. The shelf width was 50 cm. One additional control run was conducted with a vertical wall instead of the sloping bottom in order to measure the speed of

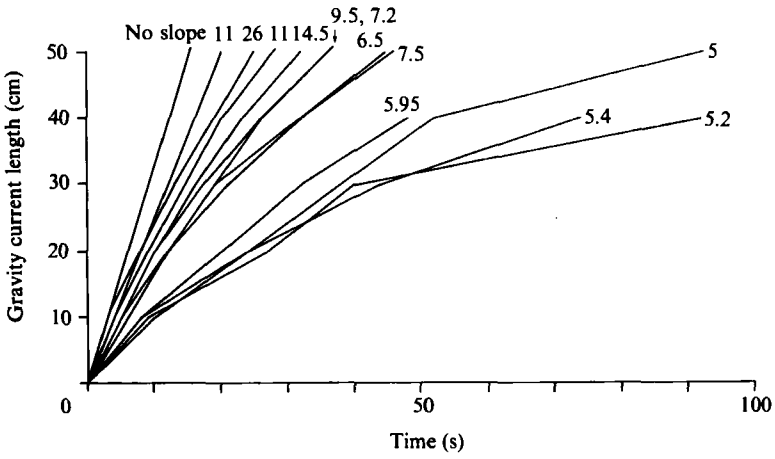

FIGURE 2. Position of the nose of the gravity current with time for the twelve runs in experiment I (from table 1). Trajectory of the gravity current along the vertical wall (no slope) is also shown. The number at the end of each curve corresponds to the rotation period of the tank in seconds.

the gravity current next to a vertical wall at distances from the source comparable to other runs. The depth and total width of the gravity current along the vertical wall were crudely measured by ruler to be 2 ± 1 cm and 3 ± 1 cm, respectively, for all runs. The depth exhibited little dependence upon rotation rate.

When the gravity current impinged on the sloping bottom, it changed dramatically by widening out and adopting a different nose velocity. Figure 2 shows displacement of the front of the nose from the bottom-outer wall intersection as a function of time for all runs. The rotation period is given at the end of each curve. Table 1 contains the physical parameters and the times at which the gravity current reached various lengths. Also plotted in figure 2 is the displacement of the nose with time for the case of no bottom slope. Three features are evident:

(i) The gravity current on the slope slowed down with time much more than the gravity current next to the vertical wall. The magnitude of slowing down was large – there were decreases in velocity of up to a factor of approximately 4.

(ii) The deceleration generally increased with decreasing rotation rate, being less than a factor of 2 at a period of 26 s and about 4 at a period of 5.4 s. (There is, of course, some dependence on g^* which may account for the non-monotonic nature of the relation.)

(iii) At rotation periods less than about 6 s, the current speed became irregular. This was associated with a more turbulent current as was evident in the photographs.

Figure 3 shows a sequence of photographs taken during a special photography run in which the gravity current was laminar and wedge shaped. For this run, Q was the same as before, while $g^* = 7.8$ cm/s^2 and $T = 10.8$ s. As the flow developed, it pushed downstream fluid ahead of it. In experiments with faster rotation rates, a stronger current was observed in front of the nose. The gravity current was still wedge shaped, but it developed some waves which, in contrast to the flow next to a vertical wall, did not separate from the current. The line of intersection of the baroclinic front with the bottom, which is visible as a dyed line on the photograph, was also wavy.

Photographs of flows at almost the fastest rotation rate of $T = 5.4$ s (figure 4) reveal that the gravity current was more eddy-like than those at slower rotation rates

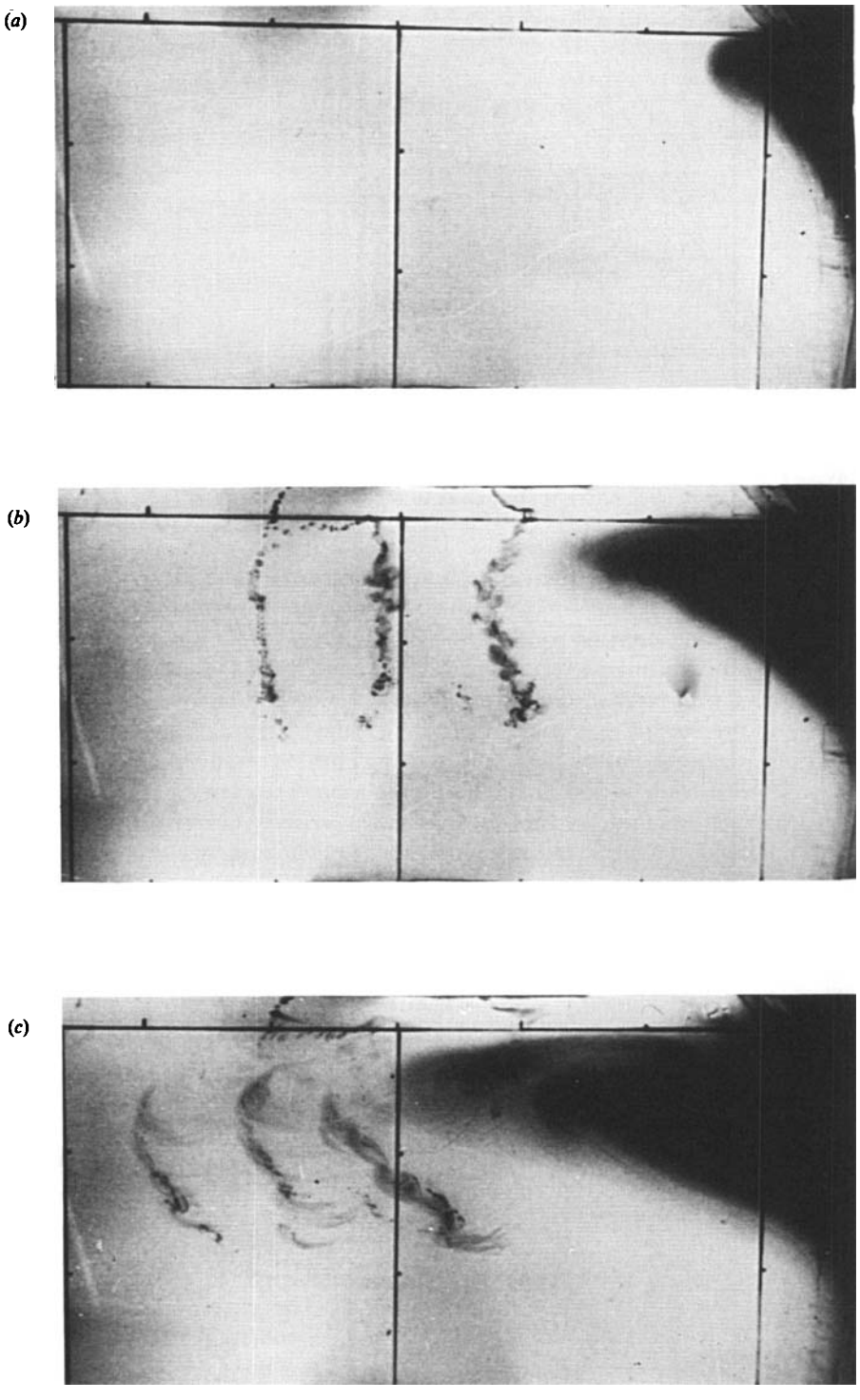

FIGURE 3. A typical laminar gravity current over a sloping bottom. The coast is toward the top. The dye streaks are slightly denser than the water in the tank and lie along the bottom. (*a*) 1 s after protruding from the wall. (*b*) 11 s later. The current is one-third of the way across the tank. The dye lines were swept downstream of the nose. (*c*) 25 s after (*a*). The wedge-shaped current is fully developed and the current ahead of the nose is also well developed.

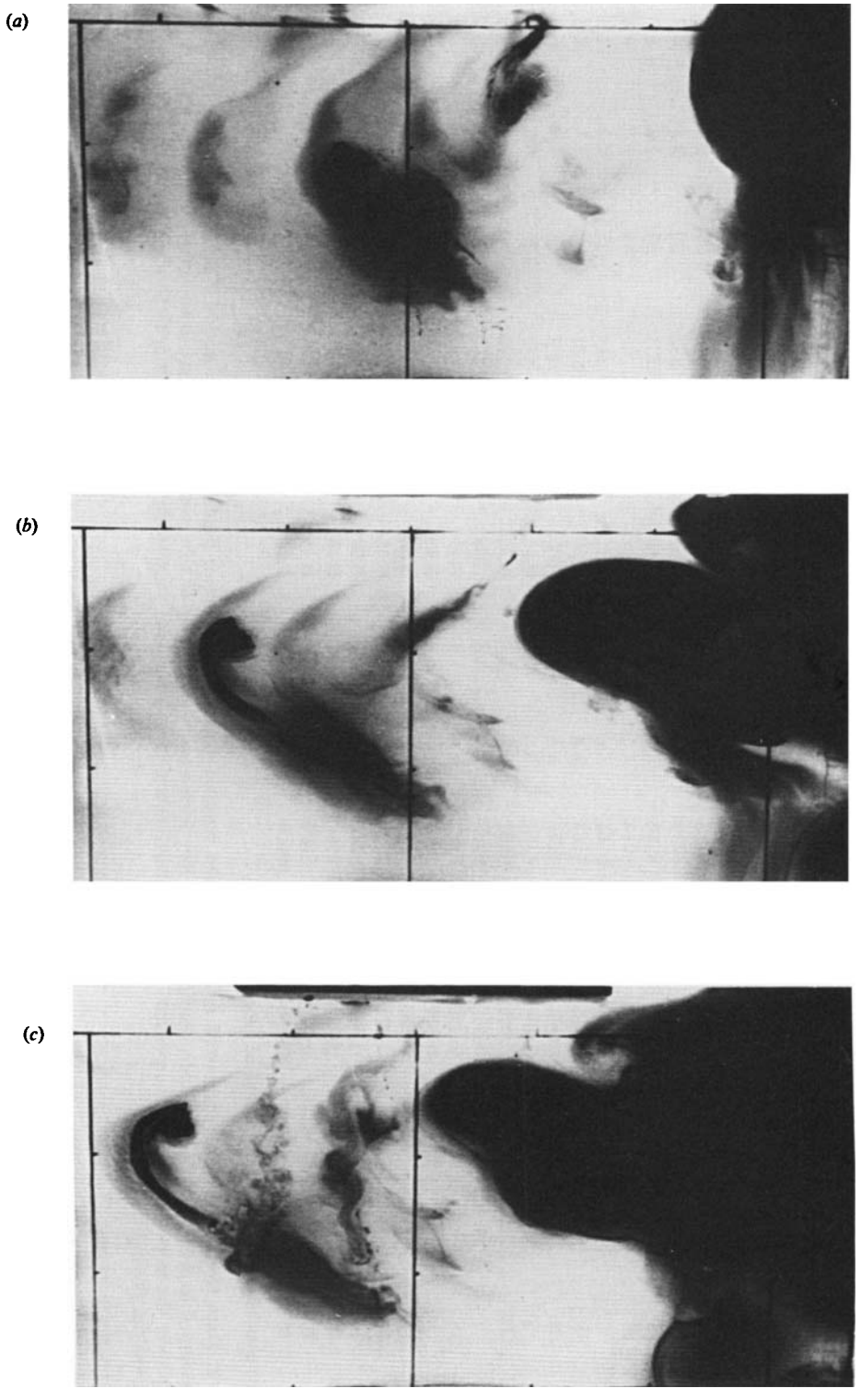

FIGURE 4. Run 3 of experiment I (see table 1). Notable features are an inability of the gravity current to penetrate to the shore, and a break-up to an eddy-like current. Times are 60, 80, and 100 s $\pm$ 1 s, respectively, after the pump was started.

Run	g^* (cm/s^2)	H (cm)	T (s)	R/L	R/H	Re	c_w (cm/s)	c_i (cm/s)	$\frac{c_w}{(g^*H)^{\frac{1}{2}}}$	$\frac{c_i}{(g^*H)^{\frac{1}{2}}}$	L_p (cm)	τ (s)	l (cm)	W (cm)
1	16	7.8	15.0	0.133	1.7	8713	7.5	7.1	0.67	0.63	421	52	3.1	12.5
2	16	7.8	12.0	0.109	1.4	8713	6.9	5.8	0.61	0.52	267	37	2.5	10.0
3	16	7.8	10.0	0.086	1.1	8713	6.8	6.2	0.61	0.54	285	39	3.1	9.3
4	16	7.8	8.0	0.071	0.91	8713	5.5	4.0	0.49	0.36	231	57	1.3	5.0
5	16	7.8	6.0	0.053	0.68	8713	4.7	2.6	0.42	0.23	164	52	1.3	6.3
6	8	7.8	15.0	0.093	1.2	6161	5.6	5.0	0.72	0.63	244	37	2.5	11.2
7	8	7.8	12.0	0.076	0.97	6161	4.4	3.2	0.56	0.41	231	67	1.3	8.1
8	8	7.8	10.0	0.063	0.81	6161	4.7	3.6	0.60	0.46	201	53	1.8	9.4
9	8	7.8	8.0	0.050	0.64	6161	3.5	1.8	0.45	0.23	233	125	0.7	6.3
10	8	7.8	6.0	0.037	0.48	6161	2.7	1.3	0.35	0.17	225	190	1.3	6.3
11	8	4.0	15.0	0.068	1.7	2263	4.9	3.8	0.88	0.68	245	64	1.3	8.2
12	8	4.0	12.1	0.056	1.4	2263	2.3	1.4	0.41	0.25	161	120	1.3	4.3
13	8	4.0	10.1	0.044	1.1	2263	NA†	1.4	NA†	0.25	140	102	1.8	6.2
14	16	4.0	15.0	0.096	2.4	3200	5.0	2.6	0.63	0.33	213	62	1.3	6.2
15	16	4.0	12.1	0.073	1.9	3200	4.4	2.6	0.55	0.33	207	78	1.3	4.4
16	16	4.0	10.4	0.068	1.7	3200	4.7	4.2	0.59	0.53	176	43	1.3	5.0
17	16	4.0	7.9	0.052	1.3	3200	3.5	2.0	0.44	0.25	190	127	1.3	4.4
18	16	4.1	6.2	0.041	0.99	3200	3.6	2.2	0.45	0.28	221	148	1.3	3.8
19	16	16.0	15.0	0.189	1.19	25600	18.5	17.2	1.15	1.08	624	31		

† Not available due to misalignment of camera.

TABLE 2. Data from experiment II. Listed for each run are reduced gravity g^*, reservoir depth H, rotation period T, ratio of Rossby radius of deformation R to shelf width L, hydrostatic number R/H, Reynolds's number $Re = (g^*H^3)^{\frac{1}{2}}/\nu$, nose velocity next to the vertical wall c_w, initial nose velocity over the sloping bottom c_i, normalized velocities, penetration length L_p, decay timescale τ, nose width next to the vertical wall l and nose width over the sloping bottom W.

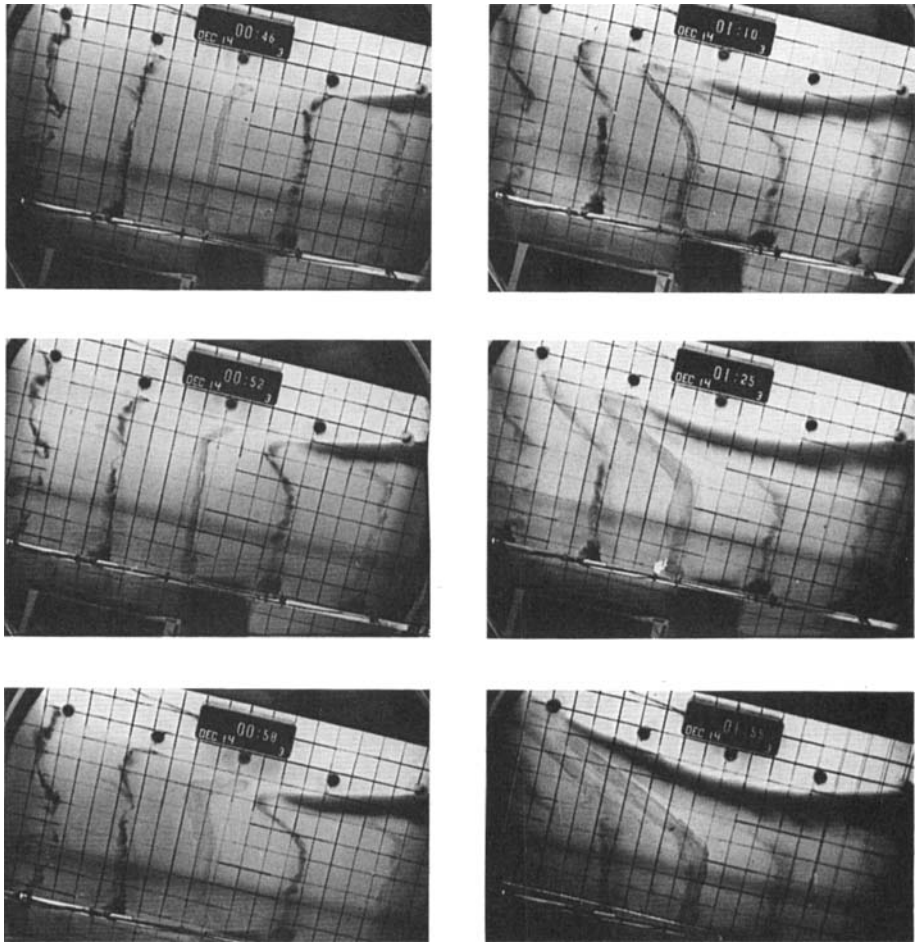

FIGURE 5. Run 4 of experiment II (see table 2). Times after opening the gate are shown on the digital clock (minutes:seconds). The current impinged on the sloping bottom at 30 s.

and it appeared to be visibly hindered by the initiation of a downstream current which developed rapidly. It surged more irregularly along the coast and did not penetrate completely to the shore.

In experiment II sixteen runs were conducted using various density differences, reservoir depths and rotation rates. (Table 2 gives the parameters and results of various measurements.) The intent was to sample the widest span of parameter space consistent with the constraints discussed at the beginning of this section. The shelf width and viscosity were fixed at $L = 100$ cm and $\nu = 0.01$ cm^2/s. A fairly typical example of the time evolution of a gravity current in experiment II is shown in figure 5. The laminar nature of the current is clear, as is the motion of the dye lines well downstream (ahead) of the nose of the gravity current.

As the gravity current encountered the sloping bottom, the most obvious quantitative change in the current was the change in the width of the nose. Figure 6(*a*, *b*) shows that total width of the nose of the current next to the vertical wall (l) and over the sloping bottom (W), each normalized by the Rossby radius of deformation R, as a function of the hydrostatic number (R/H) and of the ratio of R to the shelf width L. All measurements were taken directly from 35 mm photographs like those

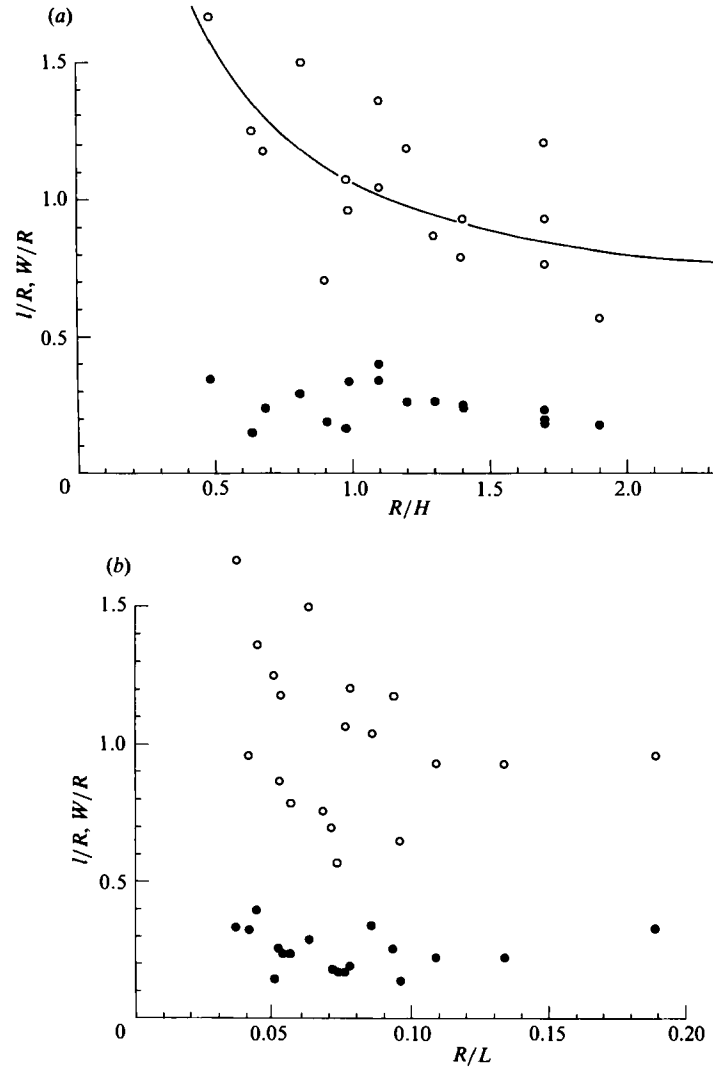

FIGURE 6. Width of the nose of the gravity current next to the vertical wall (l, solid circles) and over the sloping bottom (W, open circles) from experiment II. Each is normalized by the Rossby radius of deformation (R) and plotted as a function of the hydrostatic number (R/H) in (a) and of the ratio of R to the shelf width L in (b). The least-squares fit (4.1) is the curve in (a).

in figure 5 with an estimated error of ± 0.5 cm. W was measured soon after the current emerged from the corner, and it was always substantially greater than l. The former was generally about 1.0 R in size while the latter was about 0.2 R.

There appeared to be a systematic dependence of W/R on the hydrostatic number (figure 6a). After some trial and error with linear curve fits, the least-squares fit of

$$\frac{W}{R} = 0.51\left(\frac{R}{H}\right)^{-1} + 0.55 \tag{4.1}$$

seemed to be appropriate and is shown as the curve in figure 6(a). The correlation coefficient is 0.73, so the fit is still not very tight. However, (4.1) appears to exhibit the correct asymptotic behaviour, for as R/H becomes large, the effects of the sloping

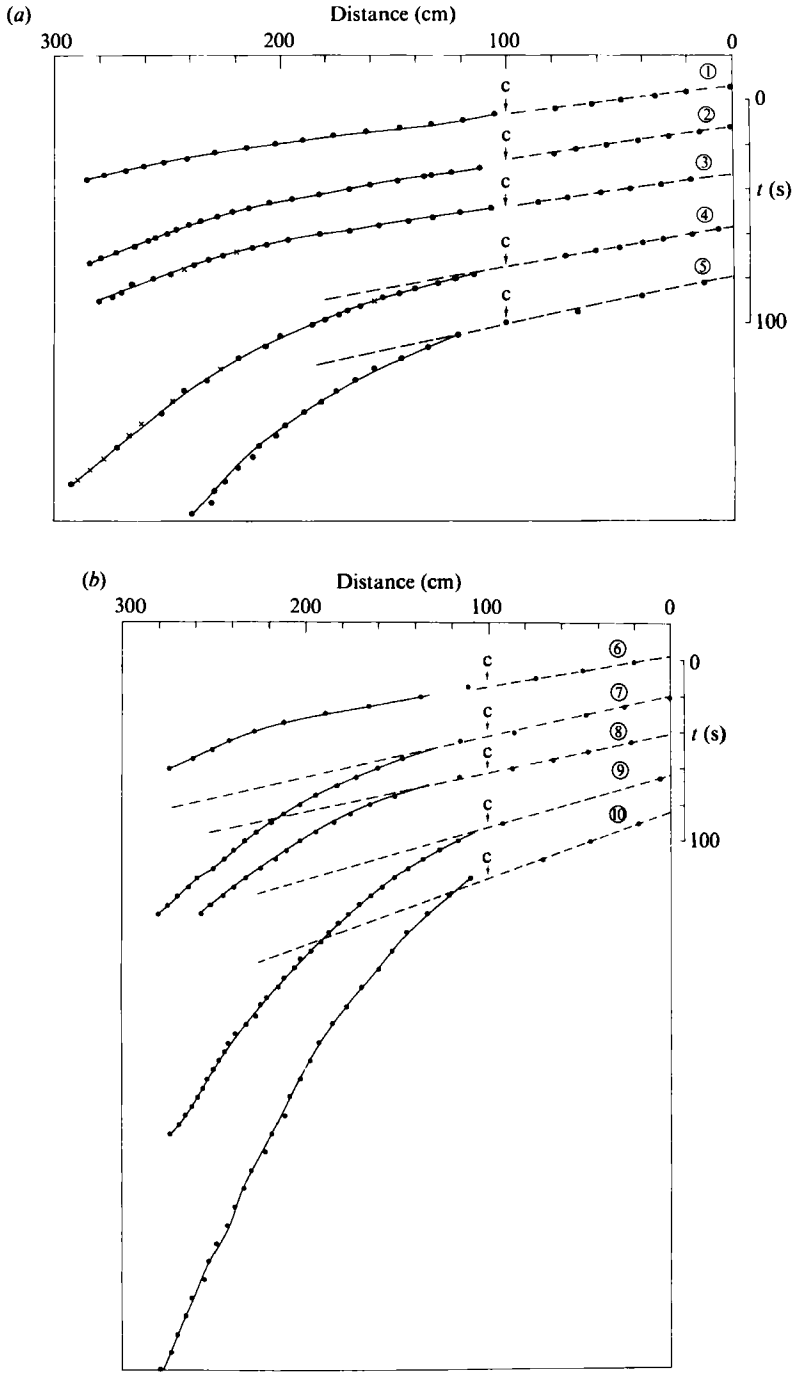

FIGURE 7. Position of the nose of the gravity current *vs.* time for the first 10 runs in experiment II [Runs 1–5 in (*a*), Runs 6–10 in (*b*)]. The removable gate is at zero distance and the sloping bottom starts at 100 cm. The timescale is shown on the right, the time origin is arbitrary. The dashed line is the linear least-squares fit to the position along the vertical wall. The transition to a coastal current over a sloping bottom begins at c and the solid curves are visual fits to the data. The solid dots are raw data points and the crosses are interpolated for analysis of the decay time.

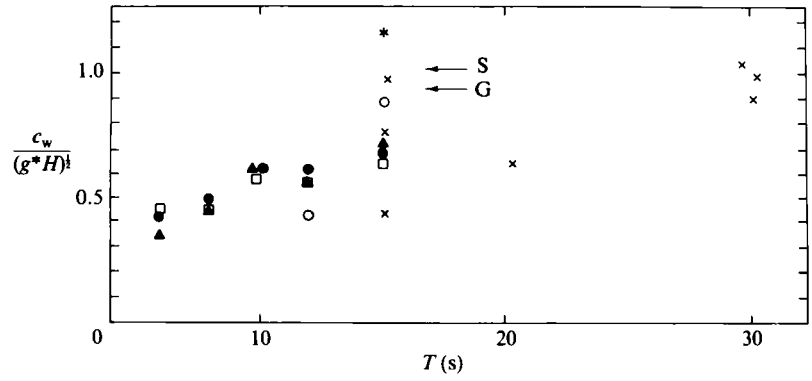

FIGURE 8. Normalized velocity of the nose of the gravity current next to the vertical wall *vs.* rotation period T from experiment II. Symbols represent different Reynolds numbers: *, $Re = 25600$; ●, $Re = 8713$; ▲, $Re = 6161$; □, $Re = 3200$; ○, $Re = 2263$. Also shown are seven data points from Stern *et al.* (×) which demonstrate similar scatter. The asymptotic velocities U_0 reported by Stern *et al.* (S) and by Griffiths & Hopfinger (G) are shown for comparison.

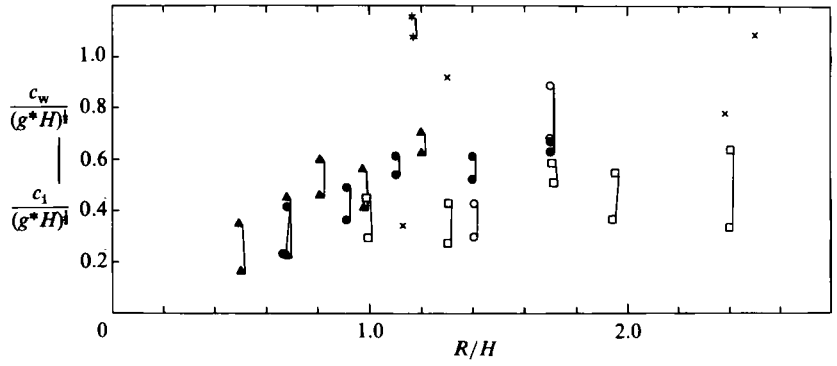

FIGURE 9. Normalized velocities next to the vertical wall (c_w, which are the upper points) and initially over the sloping bottom (c_1, which are the lower points) *vs.* hydrostatic number R/H from experiment II. Symbols represent different Reynolds numbers: *, $Re = 25600$; ●, $Re = 8713$; ▲, $Re = 6161$; □, $Re = 3200$; ○, $Re = 2263$. Four velocities from Stern *et al.* (×) are shown for comparison.

bottom are expected to decrease, and the constant 0.55 in (4.1) agrees with constants found previously [i.e. L_0 in (2.2)] for currents next to a vertical wall.

To measure velocity for each run, the position of the nose of the density current was recorded from photographs as the nose rounded the outside vertical wall, and as the nose travelled along the coast. Figure 7 shows the distance of the nose from the reservoir as a function of time for the first ten runs (with largest Reynolds numbers of 8713 and 6161, respectively). The noses travelled around the outside vertical wall with what appeared to be a constant velocity.†. After the coast was encountered, a change in velocity was observed as well as an increase in attenuation, as demonstrated by an increase in the curvature of each trajectory.

The vertical wall velocities (c_w) were estimated by a linear least-squares fit to the

† The velocity was expected to decrease as Griffiths & Hopfinger reported. However, the current encountered the sloping bottom so quickly that only a 10–20% decrease in velocity is predicted using (2.3), and this was within the accuracy of our velocity estimates.

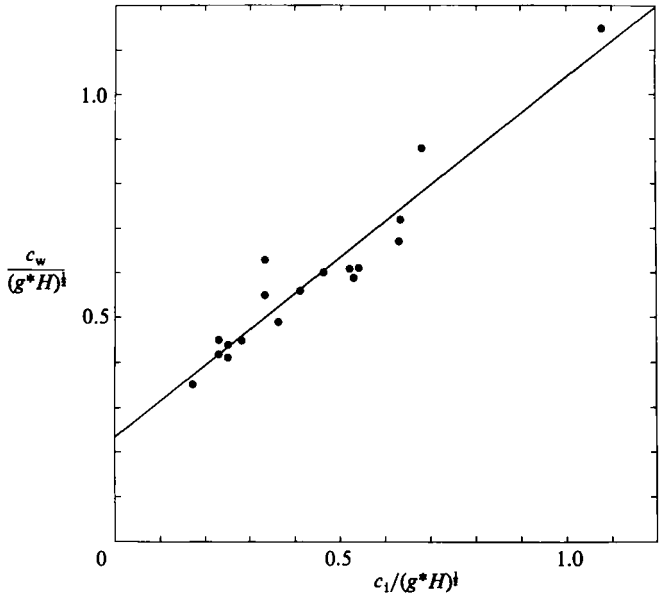

FIGURE 10. Normalized velocity next to the vertical wall (c_w) *vs.* normalized initial velocity over the sloping bottom (c_1) from experiment II. The linear least-squares fit (solid line) is $c_w/(g^*H)^{\frac{1}{2}} = 0.79\ c_1/(g^*H)^{\frac{1}{2}} + 23.4$ with a correlation coefficient of 0.96.

data and are given in table 2. They are shown in figure 8 (divided by $(g^*H)^{\frac{1}{2}}$) as a function of rotation period T. Most velocities were slower than U_0 found by Stern *et al.* (labelled S in figure 8) and by Griffiths & Hopfinger (labelled G). This difference and the large variation may be due to the smaller Reynolds numbers and hydrostatic numbers used in the present experiments. For example, a systematic increase of all velocities with increasing hydrostatic number is revealed in figure 9, which shows the wall velocity and the initial velocity over the sloping bottom (c_1) for each run (scaled by $(g^*H)^{\frac{1}{2}}$) as a function of hydrostatic number. Also shown are the velocity measurements from Stern *et al.* (their table 1) which lie in the same range, but most of their measurements were at greater values of R/H.

The systematic decrease in velocity as the shelf was encountered is also obvious in figure 9. The relationship between the wall velocity and the initial coastal velocity (figure 10) exhibited a striking linear trend, while the ratio of c_1 to c_w (figure 11) appears to be directly related to both R/H and R/L (at least for runs 1–10 and 19 which are the solid symbols). This may be expected because the effects of the sloping bottom should decrease as R increases.

The decay of the nose velocity over the sloping bottom (figure 7) has been quantified in terms of the penetration length L_p and decay time τ (table 2) by using a method developed by Mangelsdorf (1959) which is described in the Appendix. The decay time τ showed little systematic relationship to any of the dimensionless numbers. However, the penetration length L_p appeared to be linearly related to R/L as shown in figure 12. The least-squares fit (thin line) corresponds to $L_p = 2680\ R/L + 40.6$ with a regression coefficient of 0.89. The relation scaled by shelf width is $L_p/L = 26.8\ R/L + 0.41$.

In figure 12 the data for L_p are compared to the penetration length reported by Griffiths & Hopfinger (thick curve) for a gravity current next to a vertical wall [which

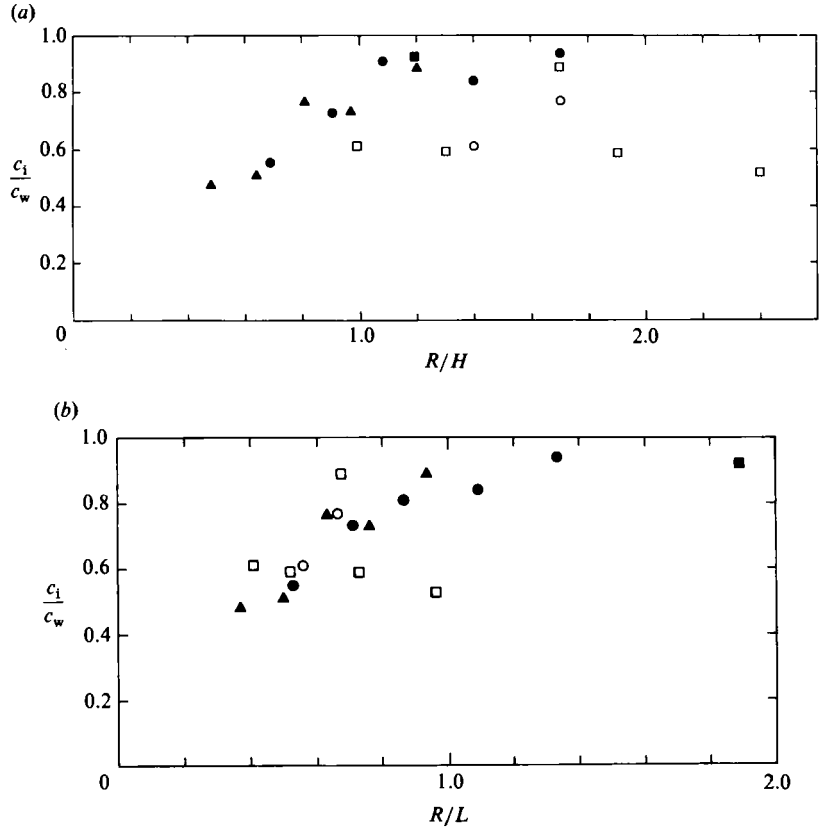

FIGURE 11. Ratio of the initial velocity over the sloping bottom (c_i) and the velocity next to the vertical wall (c_w) *vs.* (*a*) hydrostatic number, R/H and (*b*) ratio of Rossby radius of deformation to the shelf width R/L (from experiment II). Symbols represent different Reynolds numbers: ■, $Re = 25600$; ●, $Re = 8713$; ▲, $Re = 6161$; □, $Re = 3200$; ○, $Re = 2263$.

may be written $L_p = 22 \pm 4\ (RA_0)^{\frac{1}{3}}$ from (2.4)]. The gravity current over a sloping bottom has a significantly smaller penetration length than that next to a vertical wall.

4.2. *Shelf wave generation*

A particularly striking feature of experiments I and II was the current that was often initiated downstream (ahead) of the gravity current once the gravity current moved onto the sloping bottom (see figures 3 and 5). Experiment III was designed to visualize this downstream current more clearly and more quantitatively (see §3.3). Three runs were conducted in which the rotation period and the density difference were fixed at $T = 12$ s and $g^* = 8$ cm/s^2, respectively, while the reservoir depth was varied, $H = 4$, 8, 16 cm. Figures 13 and 14 show sequences of photographs from two of the runs. The downstream current is felt over the entire sloping bottom and, near the shore, is in the same direction as the gravity current. Near the offshore wall, the current appears to be slightly reversed. The displacement of the dye lines is largest near the nose of the gravity current, decreases in the downstream direction and increases with time.

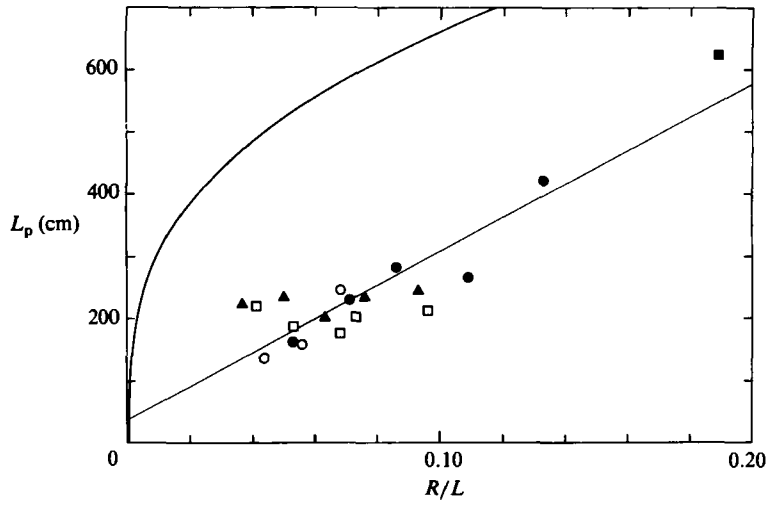

FIGURE 12. Estimated penetration length L_p *vs.* the ratio of the Rossby radius of deformation to the shelf width (from experiment II). Symbols represent different Reynolds numbers: ■, $Re = 25600$; ●, $Re = 8713$; ▲, $Re = 6161$; □, $Re = 3200$; ○, $Re = 2263$. The thick curve is the penetration length reported by Griffiths & Hopfinger (L_p in (2.4)). The thin line is a least-squares fit to the data.

These features are suggestive of barotropic shelf waves which could be forced by the gravity current provided that the nose propagates slower than some shelf-wave phase speeds. To test this idea, a theory for long barotropic shelf waves in the present geometry is developed next. Then, some considerations of forced, shelf-wave theory are presented and compared with the observations.

4.2.1. *Free shelf waves*

Following the approach of Gill & Schumann (1974), the waves are assumed to have frequencies small compared with the Coriolis parameter and wavelengths long compared with the shelf width. Under these assumptions, the inviscid, linear, vertically-averaged, shallow-water equations are

$$\left.\begin{aligned} -fv &= -g\zeta_x, \\ v_t + fu &= -g\zeta_y, \\ (uh)_x + (vh)_y + \zeta_t &= 0, \end{aligned}\right\} \tag{4.2}$$

where (x, y) are the offshore and alongshelf directions (the coast is at $x = 0$), t is time, (u, v) the (x, y) velocities, ζ the sea-surface elevation, and $h(x)$ the bottom depth (a function of x only). Subscripts (x, y, t) denote partial differentiation. Unlike the case of Gill & Schumann (1974), the surface divergence term (ζ_t) cannot be neglected because $f^2L^2/gh \approx O(1)$ in the laboratory.

The velocities can be eliminated from (4.2) to obtain a single equation for the sea-surface elevation:

$$\left(\zeta_{xx} + \frac{h_x}{h}\zeta_x - \frac{f^2}{gh}\zeta\right)_t + \frac{fh_x}{h}\zeta_y = 0. \tag{4.3}$$

Boundary conditions for the laboratory experiments are that $u = 0$ at the coast and

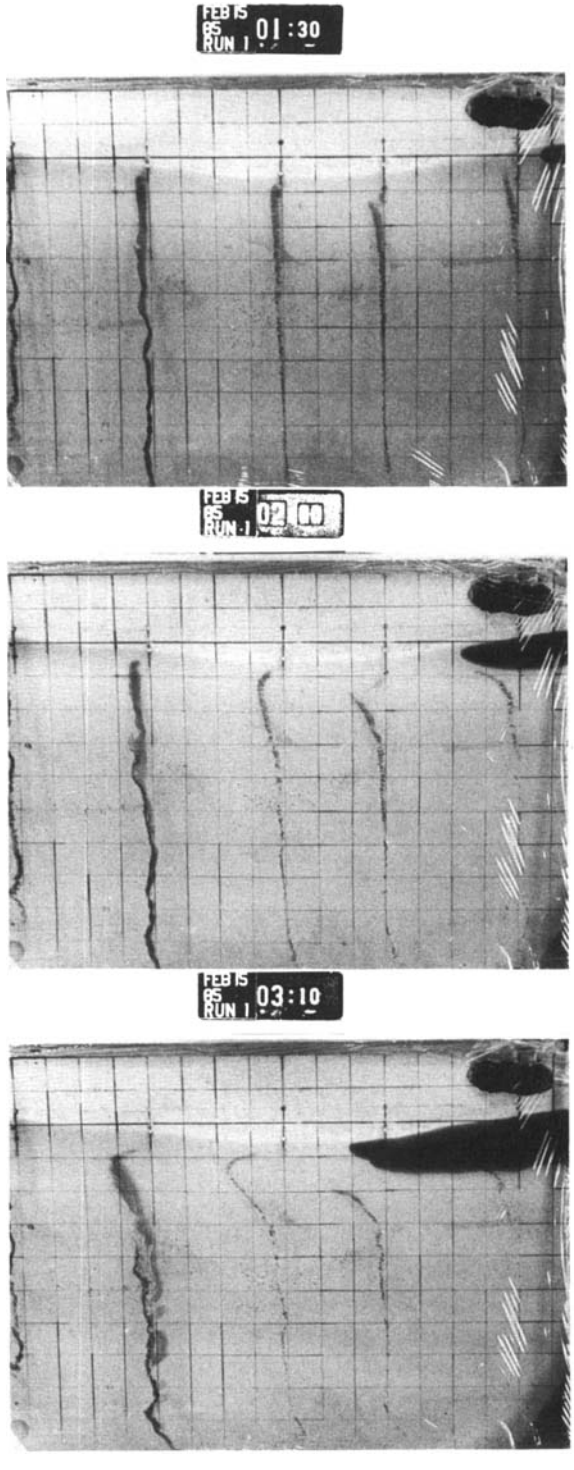

FIGURE 13. Selected photographs from experiment III with $H = 4$ cm. Times after opening the gate are shown on the digital clock (minutes:seconds).

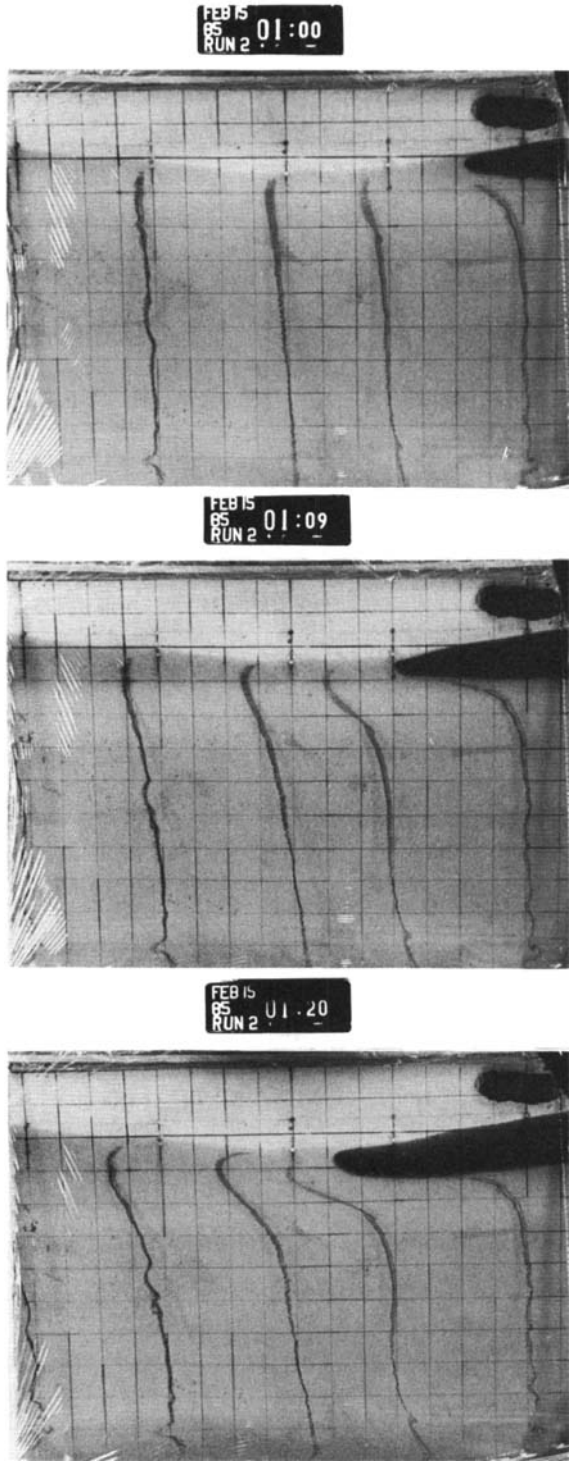

FIGURE 14. As in figure 13 but with $H = 8$ cm.

T(s)	c_0	c_1	c_2	c_3	c_4	c_5
15	84.2	12.0	4.63	2.46	1.52	1.03
12	80.4	14.5	5.72	3.05	1.89	1.29
10	76.7	16.7	6.77	3.63	2.26	1.54
8	71.4	19.6	8.26	4.48	2.81	1.92
6	63.2	23.1	10.45	5.81	3.68	2.53

TABLE 3. Phase speeds for the lowest six free shelf waves at several rotation periods computed from (4.11) using laboratory parameters $L = 100$ cm, $\alpha = 0.2$ and assuming $b = 0.1$ cm.

at the offshore wall. To prevent a singularity at the coast where $h \to 0$, the coastal boundary condition is applied at some small but finite offshore distance b. Thus,

$$\zeta_y + \frac{1}{f}\zeta_{xt} = 0 \quad \text{at } x = b, L. \tag{4.4}$$

The system (4.3) and (4.4) may be solved by separation of variables. Upon writing

$$\zeta = \sum_n F_n(x)\,\phi_n(y,t), \tag{4.5}$$

and substituting (4.5) into (4.3) and (4.4), the cross-shelf structure functions F_n are found to satisfy

$$F_n'' + \frac{h_x}{h}F_n' + \left(\frac{fh_x}{c_n h} - \frac{f^2}{gh}\right)F_n = 0, \tag{4.6}$$

$$F_n' + \frac{f}{c_n}F_n = 0 \quad \text{at } x = b, L, \tag{4.7}$$

where c_n is a separation constant and a prime denotes x differentiation. The alongshelf and time dependent functions ϕ_n each satisfy a simple first-order wave equation

$$\phi_{ny} - \frac{1}{c_n}\phi_{nt} = 0, \tag{4.8}$$

whose solution is any function of $y + c_n t$.

The laboratory topography is given by $h = \alpha x$, so (4.6) becomes

$$F_n'' + \frac{1}{x}F_n' + \frac{1}{x}\left(\frac{f}{c_n} - \frac{f^2}{g\alpha}\right)F_n = 0. \tag{4.9}$$

Solutions of (4.9) can be written

$$F_n = A\left\{J_0(\xi)\left[\frac{f}{c_n}Y_0(\xi_L) - \frac{\xi_L}{2L}Y_1(\xi_L)\right] + Y_0(\xi)\left[\frac{f}{c_n}J_0(\xi_L) - \frac{\xi_L}{2L}J_1(\xi_L)\right]\right\}, \tag{4.10}$$

where J_0, Y_0 are zero-order Bessel functions, J_1, Y_1, are first-order Bessel functions, A is an unknown amplitude, $\xi = 2(f/c_n - f^2/g\alpha)^{\frac{1}{2}}x^{\frac{1}{2}}$ and $\xi_L = \xi(L)$. Substitution of (4.10) into (4.7) yields a transcendental equation from which c_n may be determined:

$$\left[\frac{f}{c_n}J_0(\xi_b) - \frac{\xi_b}{2b}J_1(\xi_b)\right]\left[\frac{f}{c_n}Y_0(\xi_L) - \frac{\xi_L}{2L}Y_1(\xi_L)\right] - \left[\frac{f}{c_n}J_0(\xi_L) - \frac{\xi_L}{2L}J_1(\xi_L)\right]\left[\frac{f}{c_n}Y_0(\xi_b) - \frac{\xi_b}{2b}Y_1(\xi_b)\right] = 0, \tag{4.11}$$

where $\xi_b = \xi(b)$.

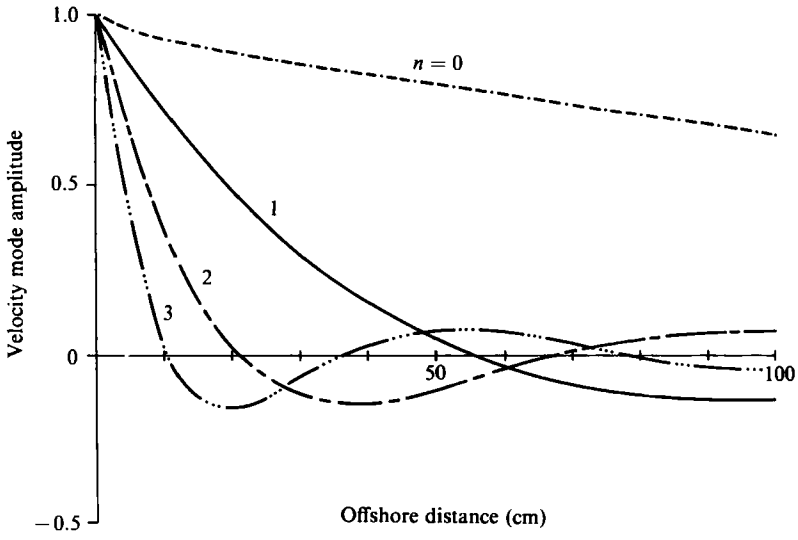

FIGURE 15. Cross-shelf structure of the displacement for modes $n = 0$–3 in equation (4.12) with $T = 12$ s and $A = -1$.

Table 3 contains phase speeds for the first six modes at various rotation periods using laboratory parameters $L = 100$ cm, $\alpha = 0.2$. The coastal boundary condition is applied at $b = 0.1$ cm, but the results are insensitive to b when $b \lesssim 1.0$ cm. The lowest mode is much faster than the other modes and corresponds to a Kelvin-like wave. The other modes are standard barotropic shelf waves but appropriate to the laboratory geometry.

The displacement of the dye lines in experiment III should be determined by the offshore structure of the alongshelf velocity (provided that the cross-shelf velocity is small). From (4.2), the alongshelf velocity structure is proportional to F'_n, which from (4.10) is

$$F'_n = -A\frac{\xi}{2x}\left\{J_1(\xi)\left[\frac{f}{c_n}Y_0(\xi_L)-\frac{\xi_L}{2L}Y_1(\xi_L)\right]+Y_1(\xi)\left[\frac{f}{c_n}J_0(\xi_L)-\frac{\xi_L}{2L}J_1(\xi_L)\right]\right\}. \quad (4.12)$$

The functions F'_n are shown in figure 15 for $n = 0$–3, a rotation period of $T = 12$ s and $A = -1$. As expected, mode zero has no zero crossings, mode one has one zero crossing, etc. The observed displacements (figures 13 and 14) typically have one zero crossing which suggests that the gravity current primarily excites the mode-one shelf wave. The zero crossings of the dye lines (figures 13 and 14) tend to be slightly farther offshore ($\approx$ 65–75 cm) than the analytical zero crossing for mode one ($= 55$ cm). This could be due to the presence of the zero-mode wave which would displace the entire dye line slightly, thus changing the apparent zero crossing. At any rate, it seems clear that the dye displacement shows little resemblance to the higher-mode structures ($n > 1$).

If the dye displacement is due to a passing shelf wave, then the displacement should start when the shelf wave arrives; a time which may be estimated based on the phase speeds listed in table 3. Observed dye line and nose positions for all runs of experiment II were plotted versus time. Figure 16 shows four clear examples. The arrows in figure 16(*a–d*) indicate the first appreciable motion of the dye while the dashed lines have slope equal to the shelf-wave phase speeds. In figure 16(*a*), the

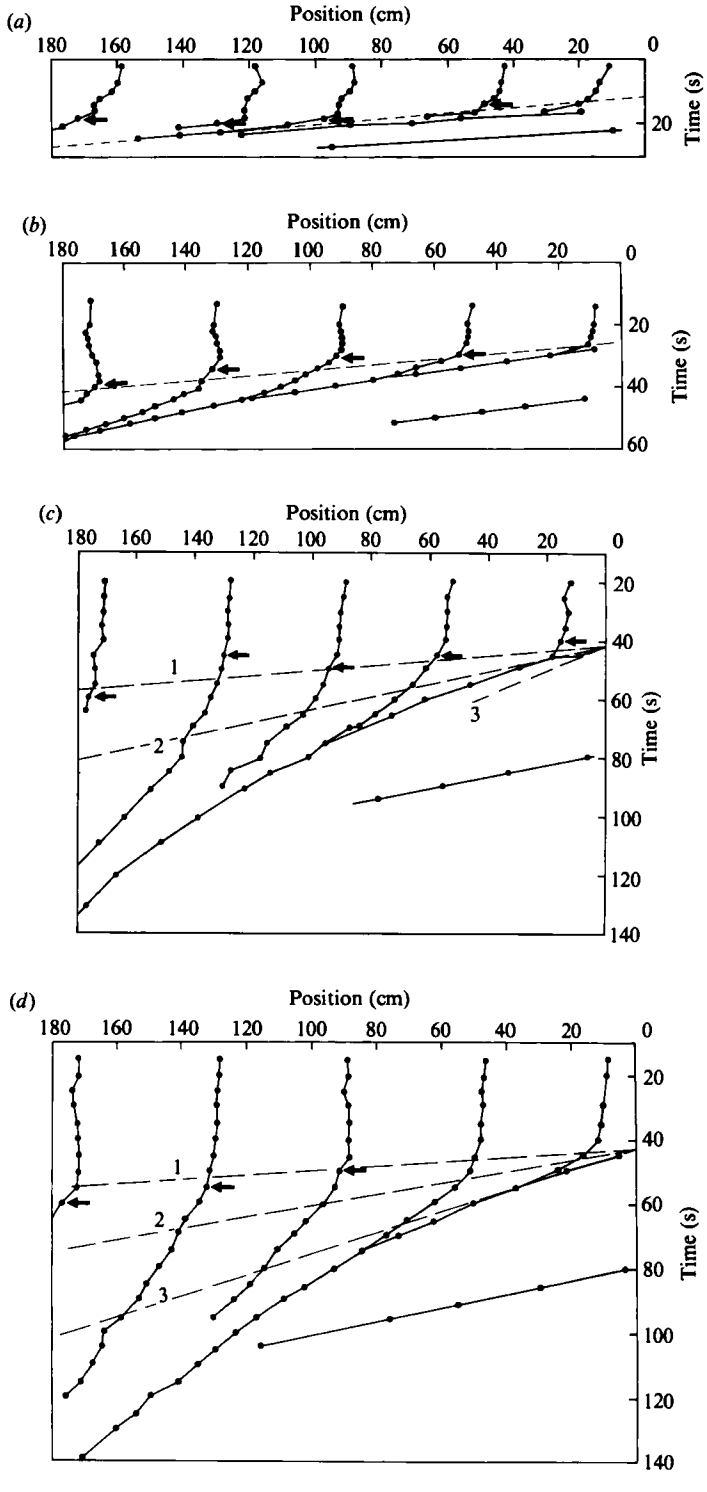

FIGURE 16 (*a–d*). For caption see facing page.

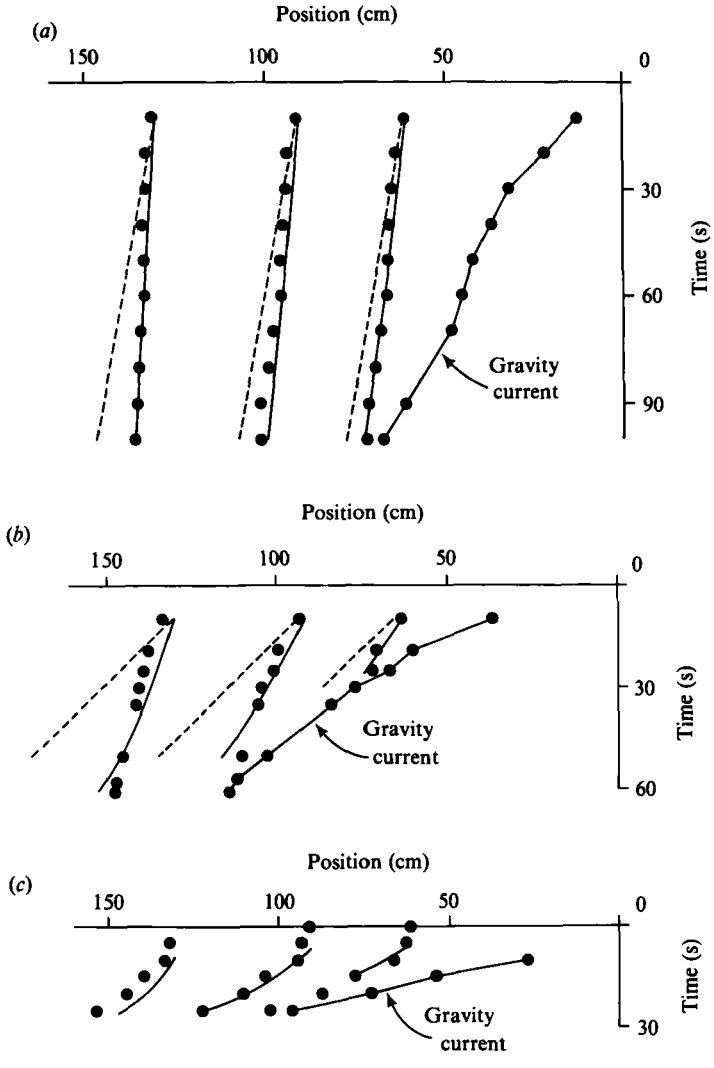

FIGURE 17. As in figure 16 but for experiment III. The solid (dashed) curves are the theoretically predicted displacements based on a forced, mode-one shelf wave with (without) bottom friction (see text for details). The gravity current speeds were approximated as (*a*) $\mu = 0.56$ cm/s, (*b*) $\mu = 1.47$ cm/s and (*c*) $\mu = 4.52$ cm/s from least-squares fits.

FIGURE 16. Nose and dye line positions (large dots connected by solid lines) *vs.* time for runs 19, 1, 11 and 7 of experiment II. Dashed lines correspond to the theoretically estimated wave speeds from table 3. Arrows indicate an estimate of the start of motion to the left by the dye. The straight line connected by dots in the lower right is the position of the gravity current next to the vertical wall before it reaches the coast. (*a*) Gravity current was faster than any shelf wave. Note that there was no attenuation of the current. (*b*) One mode was faster than the nose. There was a small amount of deceleration of the nose and clearly discerned current ahead of the nose. (*c*) Two modes were faster than the nose. The nose clearly decelerated. (*d*) Three modes were faster than the nose. The nose clearly decelerated.

gravity current travelled faster than the mode-one shelf wave, so the displacement was small until the gravity current arrived. In figure 16(*b–d*), the gravity current was slower than the first-mode shelf wave, and the arrival of the first-mode shelf wave usually coincides with a sudden change in displacement (kink in the curve) followed by a fairly steady increase in displacement with time. In figure 16(*c, d*), other shelf-wave modes could have been excited (i.e. the gravity-current speed was less than their phase speeds), but little evidence of their excitation is seen.

4.2.2. *Forced shelf waves*

If the forcing due to the gravity current could be included in (4.2) in a simple way then the theories of Gill & Schumann (1974), Brink & Allen (1978) and Clarke & Van Gorder (1986) could be applied to predict the behaviour ahead of the gravity current. Unfortunately, we have been unable to find a simple parameterization or analogue for the gravity-current forcing.†. On the other hand, if only one mode were to dominate the response (as is apparently the case here), then a single forced first-order wave equation would probably describe the result. Assuming this to be the case, the response is then described by

$$\phi_{1y} - \frac{1}{c_1}\phi_{1t} - a\phi_1 = \beta G, \tag{4.13}$$

where a is a (constant) frictional damping coefficient, and β is a (constant) coupling coefficient between the gravity-current forcing $G(y, t)$ and the first shelf-wave mode. Taking $y = 0$ to be the upstream edge of the sloping bottom (where the gravity current first meets the sloping bottom), then the solution to (4.13) is

$$\phi_1(y,t) = \beta \int_0^y G\left(\eta, t + \frac{y}{c_1} - \frac{\eta}{c_1}\right) \mathrm{e}^{a(y-\eta)}\, \mathrm{d}\eta. \tag{4.14}$$

Note that an assumption of no incident wave at $y = 0$ has been made, and that $y < 0$ in (4.14). Further, suppose that the nose of the gravity current has a constant amplitude which moves as a pulse with speed μ:

$$G(y,t) = \delta(y + \mu t), \tag{4.15}$$

where $\delta(y)$ is the Dirac delta function. Then, from (4.14),

$$\phi_1(y,t) = \frac{\beta}{1-\mu/c_1}[H(y+\mu t) - H(t+y/c_1)] \exp\left(a\left(\frac{y+\mu t}{1-\mu/c_1}\right)\right), \tag{4.16}$$

where $H(y)$ is the Heaviside step function.

Since ϕ_1 is proportional to the velocity associated with mode one, then the displacement D is proportional to the time integral of ϕ_1. From (4.16)

$$D = \int_0^t \phi_1(y,t')\, \mathrm{d}t' = \frac{-\beta}{a\mu}\left\{H\left(t + \frac{y}{c_1}\right)\left[\exp\left(a\left(\frac{y+\mu t}{1-\mu/c_1}\right)\right) - \exp(ay)\right]\right.$$
$$\left. - H(y+\mu t)\left[\exp\left(a\left(\frac{y+\mu t}{1-\mu/c_1}\right)\right) - 1\right]\right\}. \tag{4.17}$$

† An analogue to the wind-forced problem with bottom friction and full mode coupling (as in Clarke & Van Gorder 1986) was solved in which the nose of the gravity current was modelled as a moving pulse of wind stress with a step function offshore structure. The results were not encouraging due to the strong excitation of high shelf-wave modes. It was concluded that the coupling of the wind to the shelf waves is very different from the coupling of the gravity current to the shelf waves. The approach was subsequently abandoned.

If bottom friction were negligible ($a \to 0$), then

$$D = \frac{\beta}{1-\mu/c_1}\left\{H(y+\mu t)\left(t+\frac{y}{\mu}\right) - H\left(t+\frac{y}{c_1}\right)\left(t+\frac{y}{c_1}\right)\right\}. \tag{4.18}$$

Provided that the gravity current speed is less than the shelf-wave speed ($\mu < c_1$), then the dye displacement at $y = y_0$ starts when the shelf wave reaches y_0 and continues almost linearly with time (exactly linearly with time if $a = 0$). Thus, the displacement occurs earlier in time at upstream positions and is always larger there (consistent with figures 13 and 14).

This displacement from (4.17) has been compared to the observed displacement of dye lines in each run of experiment III. The procedure was to estimate the speed of the gravity current μ, assume $a = 0.01$ cm^{-1} and match the solution of (4.17) at a *single* point in space and time. The matching is necessary because there is no way to compute the coupling coefficient β.

The results are shown in figure 17. The circles are the locations of the dye lines (at approximately 20 cm offshore) and the nose of the gravity current at various times (as in figure 16). The solid lines are the prediction from (4.17) while the dashed lines in figure 17 (*a*, *b*) are the frictionless result ($a = 0$ in (4.18)) for comparison. In each case, the qualitative agreement is good, but the quantitative agreement deteriorates somewhat for the faster gravity currents (figure 17*b*, *c*). The importance of bottom friction, however, seems indisputable.

In summary, the current which occurs ahead of the gravity current over the sloping bottom has structure and growth properties which are consistent with the idea that the gravity current excites the frictionally damped, first-mode, barotropic shelf wave whenever the shelf-wave phase speed is greater than the gravity-current speed. Apparently, higher shelf-wave modes are not highly excited or are highly damped.

5. Conclusion

A gravity current over a uniformly sloping bottom readjusts to be wider, slower, more laminar and more rapidly decelerating than a gravity current next to a vertical wall. When the gravity current moves slower than the first-mode barotropic shelf wave, energy is radiated ahead of the nose, a process which bleeds energy out of the density current and contributes to its deceleration. Other factors such as viscous drag and a limited source of light fluid also contribute to the deceleration, however, the relative importance of each remains an open question.

Thanks are due especially to Robert Frazel who constructed the apparatus and produced the excellent photographs. Robert Beardsley made important suggestions for improving the analysis and the text. JAW was funded by the Office of Naval Research under ONR Contract N00014-82-C-0019, NR 083-004. DCC was funded by the National Science Foundation grants OCE80-14941 and OCE84-17769, contribution number 5851 of Woods Hole Oceanographic Institution.

Appendix. The Mangelsdorf method of estimating exponential decay

This is an easy and efficient method of estimating exponential decay from data taken at equal time intervals. Let the nth data point be

$$Y_n = A + B\,\mathrm{e}^{-\alpha t_n},$$

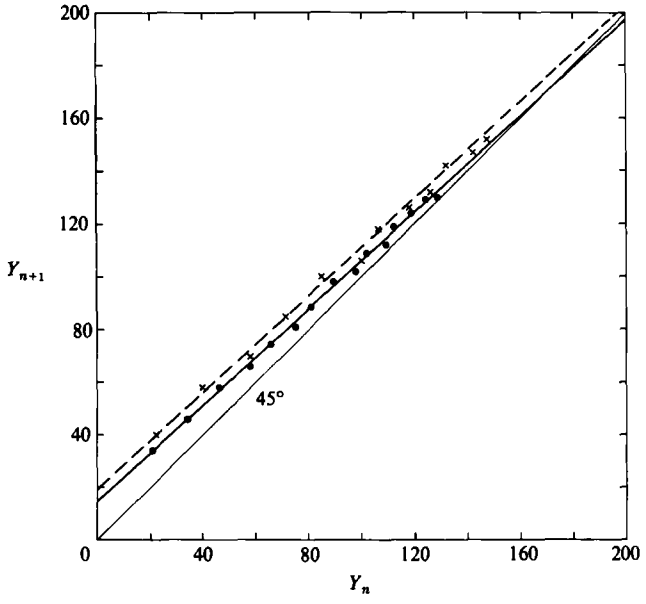

FIGURE 18. Data from runs 1 and 2 of experiment II, plotted as sequential points for fitting to an exponential using the Mangelsdorf method (see Appendix).

and the $(n+1)$th data point be taken Δt later

$$Y_{n+1} = A + B\,\mathrm{e}^{-\alpha(t_n+\Delta t)}.$$

Thus, $(Y_{n+1}-A) = (Y_n-A)\,\mathrm{e}^{-\alpha\Delta t}$ and the slope of Y_{n+1} plotted versus Y_n is $\mathrm{e}^{-\alpha\Delta t}$. The penetration length A (as $t\to\infty$) is the intersection with the 45° line.

The data from runs 1 and 2 of experiment II (also shown in figure 5*a*) are plotted in figure 18 using this method. The points fall on nearly straight lines which intersect with the 45° line ($Y_{n+1} = Y_n$) at clearly defined places. The regression coefficients for the linear least-squares fits were greater than 0.998 for all 16 runs of experiment II. This is how the penetration length L_p and decay timescale τ shown in table 2 were estimated.

REFERENCES

BRINK, K. H. & ALLEN, J. S. 1978 On the effect of bottom friction on barotropic motion over the continental shelf. *J. Phys. Oceanogr.* **8**, 919–922.

CLARKE, A. J. & VAN GORDER, S. 1986 A method for estimating wind driven shelf and slope water flow. *J. Phys. Oceanogr.* **16**, 1011–1026.

GILL, A. E. & SCHUMANN, E. H. 1974 The generation of long shelf waves by the wind. *J. Phys. Oceanogr.* **4**, 83–90.

GRIFFITHS, R. W. & HOPFINGER, E. J. 1983 Gravity currents moving along a lateral boundary in a rotating fluid. *J. Fluid Mech.* **134**, 357–399.

MANGELSDORF, P. C. 1959 A convenient plot for exponential functions with unknown asymptotes. *J. Appl. Phys.* **30**, 442.

MORK, M. 1981 Circulation phenomena and frontal dynamics of the Norwegian coastal current. *Phil. Trans. R. Soc. Lond.* A **302**, 635–647.

SIMPSON, J. E. 1982 Gravity currents in the laboratory, atmosphere, and ocean. *Ann. Rev. Fluid Mech.* **14**, 213–234.

STERN, M. E. 1980 Geostrophic fronts, bores, breaking and blocking waves. *J. Fluid Mech.* **99**, 687–703.

STERN, M. E., WHITEHEAD, J. A. & HUA, B.-L. 1982 The intrusion of a density current along the coast of a rotating fluid. *J. Fluid Mech.* **123**, 237–265.